

Supplemental Material for

Plasmonic Vortices Host Magnetoelectric Interactions

Atreyie Ghosh,¹ Sena Yang,¹ Yanan Dai,^{1,2,3} W. Vincent Liu,¹ Hrvoje Petek^{1*}

¹Department of Physics and Astronomy, University of Pittsburgh and IQ Initiative, Pittsburgh, PA 15260, USA

²Department of Physics, Southern University of Science and Technology (SUSTech), Shenzhen, 518055, China

³Quantum Science Center of Guangdong-Hong Kong-Macao Greater Bay Area (Guangdong), Shenzhen, 518045, China

Quantifying A_{ME} in Hexagonal Plasmonic Vortex Array

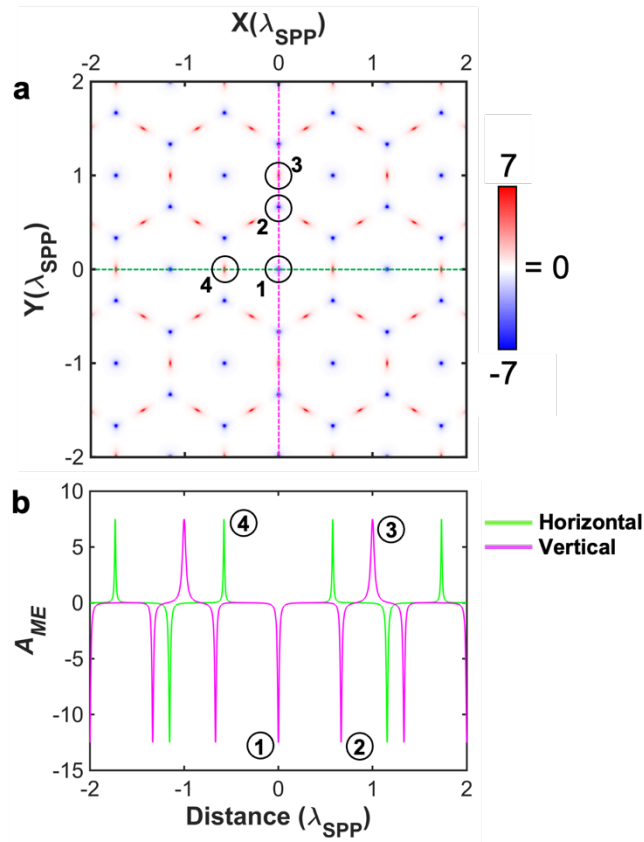


Fig. S1: Quantifying the ME density of a hexagonal vortex array. **a**, The ME density (A_{ME}) for $\delta = 10^{-4}$ and $\lambda_{SPP} = 530$ nm. **b**, The horizontal and vertical line profiles of A_{ME} along the green and purple dashed lines of **a**, represented by the associated colors. The height magnitudes and full width half maxima (FWHM) (in nm scale), of the different peaks denoted by ①, ②, ③, ④ at the spatial locations indicated by the same numbers in **a** are [12.5; 12.5, 7.5, 7.5] and [10.3, 10.1, 22.5, 7.4], respectively.

As noted in the main text, the localization of the magnetoelectric response (A_{ME}) is not spatially uniform for polygonal coupling structures with $Q \geq 5$ because of frustration of interaction of dipolar light with polygonal CS. Fig. S1a shows the calculated A_{ME} distribution for $Q = 6$ using the same λ_{SPP} and δ as in Fig. 2b, but over a larger spatial region. The horizontal and vertical line profiles of A_{ME} along the green and purple dashed lines of Fig. S1a, respectively, are plotted in Fig. S1b with the corresponding colors. The central peak profiles overlap in the horizontal and vertical directions. For $Q=6$ there are two vortex lattices with consistent A_{ME} within each lattice, though with the opposite sign, different amplitudes, and full widths at half maxima (FWHM) between them.

Quantifying A_{ME} As Function of Polygon Sides

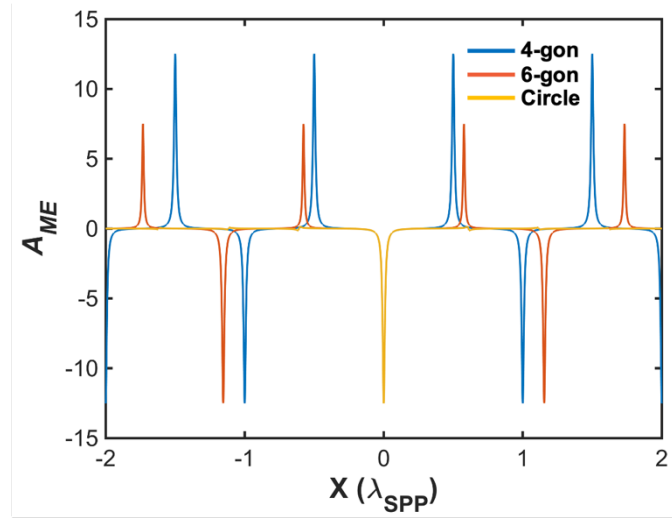


Fig. S2: Quantifying A_{ME} for CS with different polygon sides. The horizontal line profiles of A_{ME} across the central vortex for $Q=4$, $Q=6$, and circle CS with $\delta = 10^{-4}$ and $\lambda_{SPP} = 530$ nm. The central A_{ME} peak is identical for CS with different Q . The heights and FWHM of the peaks are already reported in Fig. 2 and Fig. S1.

Fig. S2 presents the horizontal line profiles of A_{ME} for different polygonal CS ($Q = 4$, $Q = 6$, and circle) over a longer distance than in Fig. 2b. The plot implies that A_{ME} at the central vortex

is independent of Q . As the surrounding vortex distributions vary for different Q , the localization of is also A_{ME} distinct, as evident in Fig. S2.

Chiral Density of Square Vortex Array

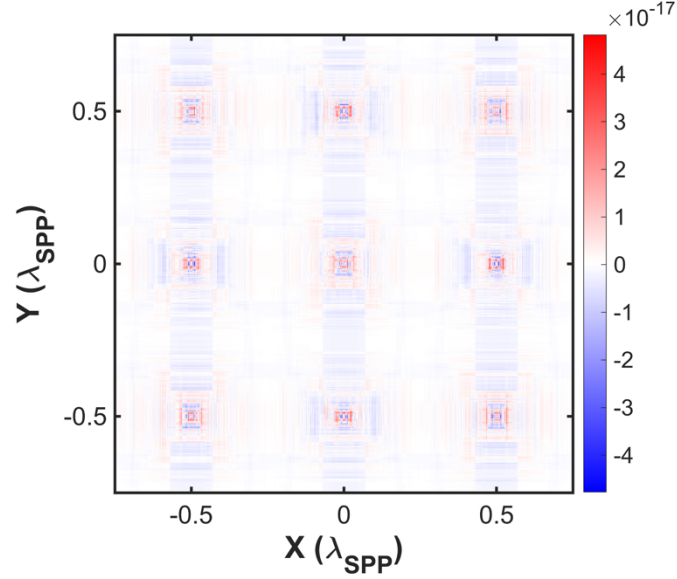


Fig. S3: The chiral density C_{ME} of the square vortex array. The chiral density C_{ME} is calculated for same spatial region as shown as in Fig. 2b. Note the exponent of the color scale, which can only be interpreted as digital noise in the calculation. It is therefore evident that $C_{ME} \sim 0$ at plasmonic vortex cores.

Fig. S3 shows the distribution of the chiral density C_{ME} of the square plasmonic vortex array for the same spatial region as in Fig. 2b. The result $C_{ME} \sim 0$ is expected for an evanescent wave because it is given by the projection of the SPP helicity onto $k_{SPP}[1]$, which is zero. Therefore, for plasmonic vortices, C_{ME} vanishes, and A_{ME} dominates at vortex cores. The obtained values for C_{ME} in Fig. S3 are at the noise level of the digital calculation.

Extraction of Vectorial SPP Field Components

Fig. S4a shows the PEEM image where 2PP signal is excited with a train of single ~ 20 fs pulses, which produce a target-like pattern that is created by interferences affecting SPP fields that emanate from the circular CS with an accumulated 2π phase shift per each optical cycle. The target

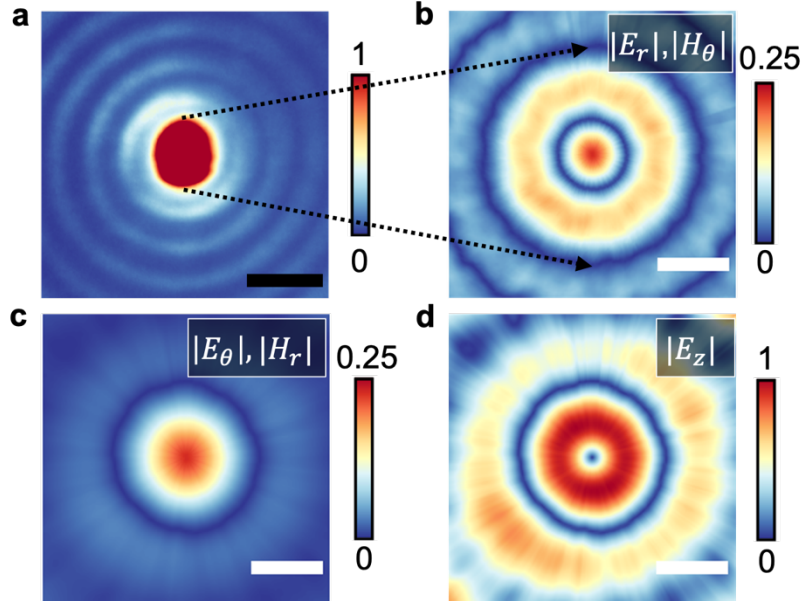


Fig. S4: Ultrafast microscopy of E , H , and E - H fields at a circular plasmonic vortex core. **a**, PEEM image of 2PP spatial distribution from a polycrystalline Ag film with a lithographically etched circular CS that is excited with a single pulse train of ultrafast LCP laser pulses. The circular CS generates an SPP plasmonic vortex with a skyrmion spin texture (from Ref. [2]). The SPP fields gyrate at $\omega_L=0.54$ PHz frequency, with anti-parallel alignment of \mathbf{E} and \mathbf{H} over the 20-fs pulse duration in the central region (Fig. 1). This creates a concentric circle target interference pattern. The scale bar indicates $2\lambda_{SPP}$ (1060 nm). **b-d**, Different \mathbf{E} - and \mathbf{H} -cylindrical field components of the same vortex core extracted from ITR-PEEM measurements by pump-probe excitation. The ITR-PEEM imaging and analysis of the \mathbf{E} - and \mathbf{H} -field components shows the in-plane field focus and out-of-plane E_z phase singularity at the vortex core. The white scale bars in **b-d** denote $\lambda_{SPP}/2$ (265 nm). The color scales represent the normalized experimentally extracted 2PP signal intensity in **a** and the normalized amplitude absolute value distributions of the field components.

pattern with an intense $\sim \lambda_{SPP}/2$ diameter focus centered on the vortex core forms by integrating the 2PP signal over the pulse duration from the spiraling SPP wavefront. In two pulse pump-probe excitation experiments, as described by Dai *et al.*[2], different SPP field component-induced 2PP signals can be obtained by Fourier filtering time-domain ITR-PEEM image sequence[3,4]. The Fourier filtered image sequences, thereby, generate a phase dependent movie of the E_r SPP field component that oscillate at the laser driving frequency (ω_L). The remaining \mathbf{E} and \mathbf{H} field components in Fig. S4b-d are calculated from the E_r field based on Maxwell's equations. A further detailed discussion of vectorial imaging of plasmonic fields can be found references [2,5,6]. Note that the spatial distributions of \mathbf{E} and \mathbf{H} fields, $E_r \sim H_\theta$ and $E_\theta \sim H_r$, are identical and have a strong

focus at the vortex core, where the vortex phase singularity sets $E_z \sim 0$. The measured $|\mathbf{E}^* \cdot \mathbf{H}|$ and $|A_{ME}|$ distributions at the circular vortex core of Fig. 4 are determined by these field distributions.

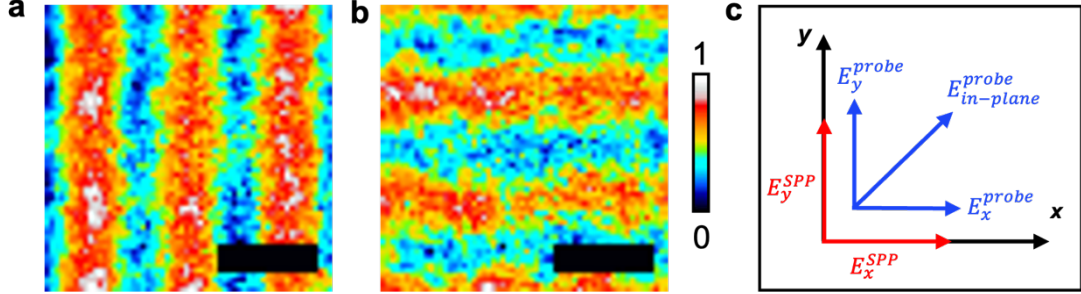


Fig. S5: The Fourier filtered 2PP signal due to SPP field components. **a**, E_x and **b**, E_y field components are obtained from the experimental data of a square CS array of SPP vortices from the ITR-PEEM experiment reported in Ref.[7]. The scale bars indicate λ_{SPP} . The color scale represents normalized photoelectron counts given by the nonlinear interaction of each field component. **c**, Vector fields in x - y directions are obtained by interference between orthogonal SPP fields and the component of in-plane probe field, which is parallel to them.

The 4-fold symmetry of a square SPP CS enables the in-plane SPP $\mathbf{E}_{||}$ field to be decomposed into two orthogonal standing waves in the x and y directions; their unnormalized amplitude oscillates in space, but does not propagate. Because in ITR-PEEM experiment, we record the in-plane fields through Fourier processing of raw data, the 2PP signals due to plasmon E_x and E_y fields of Fig. S5 can be considered as two linearly polarized signals being imaged by the PEEM. Since the generated SPP fields serve as two orthogonally polarized fields in x and y directions, when using circularly polarized light (CPL) pulses as a probe that contains field components along x and y directions, selective interference with the SPP field along either x or y direction is obtained (Fig. S5c). This is experimental geometry for the vectorial field imaging[8].

Due to symmetry of the co-ordinate system, for the circular and square CS, the absolute and real values of $(\mathbf{E}^* \cdot \mathbf{H})$ are experimentally extracted, respectively. For the circular vortex in Fig. 2, $(\mathbf{E}^* \cdot \mathbf{H})$ has either negative or positive values depending on the helicity of the excitation field, while $Im(\mathbf{E}^* \cdot \mathbf{H}) \sim 0$ (Fig. S3). Hence, $|\mathbf{E}^* \cdot \mathbf{H}|$ and $Re(\mathbf{E}^* \cdot \mathbf{H})$ are identical quantities.

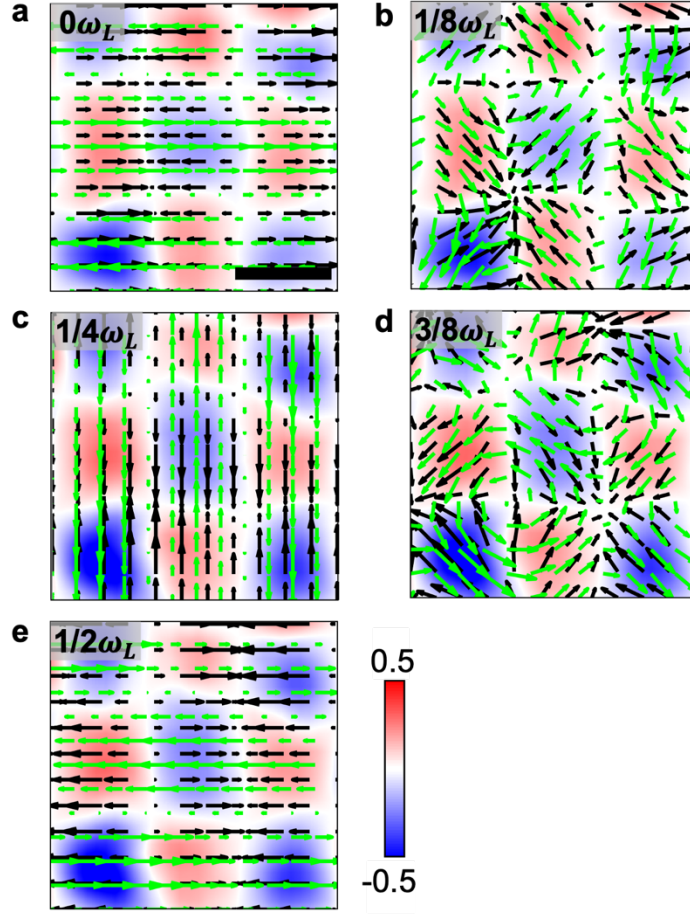


Fig. S6: Ultrafast microscopy of vectorial fields for a square plasmonic vortex array. **a-e**, Color maps represent the experimental $Re(\mathbf{E}^* \cdot \mathbf{H})$ distribution and black and green arrows denote, respectively, the experimentally defined polarization of the gyrating SPP $\mathbf{E}_{||}$ and $\mathbf{H}_{||}$ fields over one-half of an optical cycle. The vectorial $\mathbf{E}_{||}$ and $\mathbf{H}_{||}$ field components are extracted from the experimental data for the square vortex array as demonstrated in Fig. S5. Their respective parallel and antiparallel projections define the red (positive) and blue (negative) $Re(\mathbf{E}^* \cdot \mathbf{H})$ values. The scale bar in **a** indicates $\lambda_{spp}/2$ (265 nm) for every image.

The color scale in Fig. S6a-e shows images at a specific pump-probe delays of the experimentally extracted $Re(\mathbf{E}^* \cdot \mathbf{H})$ of the square vortex array, along with the amplitudes and phases of the extracted SPP $\mathbf{E}_{||}$ and $\mathbf{H}_{||}$ fields represented by black and green arrows, respectively. By advancing τ in $1/8$ of an-optical cycle steps (~ 0.23 fs), the optical and SPP field phases advance by $\pi/4$, such that the $\mathbf{E}_{||}$ and $\mathbf{H}_{||}$ fields rotate by 45° (Fig. S6b); additional advances in $\pi/4$ steps cause the fields to rotate accordingly (Fig. S6c and S6d), so that after $1/2\omega_L$ advance they point in the opposite direction (Fig. S6e) with respect to the start in Fig. S6a.

Movies

The analytically calculated femtosecond co-gyration of the \mathbf{E}_{\parallel} and \mathbf{H}_{\parallel} fields at the cores of the circular vortex (**Movie S1**) and square vortex array (**Movie S2**). Color maps (same range as shown in Fig. 2b) represent $Re(\mathbf{E}^* \cdot \mathbf{H})$ distribution, while the black and green arrows indicate the SPP \mathbf{E}_{\parallel} and \mathbf{H}_{\parallel} fields, respectively. Each movie evolves over one optical cycle time scale (~ 1.83 fs).

The scale bars indicate $\lambda_{SPP}/2$.

- [1] F. Alpegiani, K. Y. Bliokh, F. Nori, and L. Kuipers, Electromagnetic Helicity in Complex Media, *Physical Review Letters* **120**, 243605 (2018).
- [2] Y. Dai, Z. Zhou, A. Ghosh, K. Kapoor, M. Dąbrowski, A. Kubo, C.-B. Huang, and H. Petek, Ultrafast microscopy of a twisted plasmonic spin skyrmion, *Applied Physics Reviews* **9**, 011420 (2022).
- [3] G. Spektor, D. Kilbane, A. K. Mahro, M. Hartelt, E. Prinz, M. Aeschlimann, and M. Orenstein, Mixing the Light Spin with Plasmon Orbit by Nonlinear Light-Matter Interaction in Gold, *Physical Review X* **9**, 021031 (2019).
- [4] Y. Dai, Z. Zhou, A. Ghosh, R. S. K. Mong, A. Kubo, C.-B. Huang, and H. Petek, Plasmonic topological quasiparticle on the nanometre and femtosecond scales, *Nature* **588**, 616 (2020).
- [5] Y. Dai, Z. Zhou, A. Ghosh, S. Yang, C.-B. Huang, and H. Petek, Ultrafast nanofemto photoemission electron microscopy of vectorial plasmonic fields, *MRS Bulletin* **46**, 738 (2021).
- [6] M. Dąbrowski, Y. Dai, and H. Petek, Ultrafast Photoemission Electron Microscopy: Imaging Plasmons in Space and Time, *Chemical Reviews* **120**, 6247 (2020).
- [7] A. Ghosh, S. Yang, Y. Dai, Z. Zhou, T. Wang, C.-B. Huang, and H. Petek, A topological lattice of plasmonic merons, *Applied Physics Reviews* **8**, 041413 (2021).
- [8] T. J. Davis, D. Janoschka, P. Dreher, B. Frank, F.-J. Meyer zu Heringdorf, and H. Giessen, Ultrafast vector imaging of plasmonic skyrmion dynamics with deep subwavelength resolution, *Science* **368**, eaba6415 (2020).